Title

Three-dimensional full-loop simulation of a dual fluidized-bed biomass gasifier

Journal

Applied Energy, 160(C)

ISSN

0306-2619

Authors

Liu, Hui

Cattolica, Robert J

Seiser, Reinhard

et al.

Publication Date

2015-12-01

DOI

10.1016/j.apenergy.2015.09.065

Peer reviewed

Applied Energy 160 (2015) 489–501

Contents lists available at ScienceDirect

Applied Energy

journal homepage: www.elsevier.com/locate/apenergy

Three-dimensional full-loop simulation of a dual fluidized-bed biomass gasifier

Hui Liu [a], Robert J. Cattolica [a,*], Reinhard Seiser [a], Chang-hsien Liao [b]

[a] Department of Mechanical and Aerospace Engineering, University of California, San Diego, 9500 Gilman Drive, La Jolla, CA 92093, USA
[b] West Biofuels, LLC, Woodland Biomass Research Center, 14958 County Road 100B, Woodland, CA 95776, USA

HIGHLIGHTS

- CFD simulation of biomass gasification in a dual fluidized-bed.
- The CFD model predicts the gas composition and the reactor temperature distribution.
- The CFD model has been validated by experimental data.
- The effects of the particle size distribution and drag models have been investigated.

ARTICLE INFO

Article history:
Received 12 May 2015
Received in revised form 10 September 2015
Accepted 15 September 2015

Keywords:
Biomass gasification
Fluidization
CFD modeling

ABSTRACT

A three-dimensional CFD model was developed to simulate the full-loop of a dual fluidized-bed biomass gasification system consisting of a gasifier, a combustor, a cyclone separator, and a loop-seal. This full-loop simulation includes the chemical kinetic modeling of biomass drying and pyrolysis, heterogeneous char reactions, and homogeneous gas-phase reactions. In the model, the gas phase is described using Large Eddy Simulation (LES) and the particle phase is described with the Multiphase Particle-In-Cell (MP-PIC) method. The simulation was performed using the GPU-accelerated computing and the simulation results were compared with the gas composition and temperature measurements from a pilot-scale biomass gasification power plant (1 MW_{th}, 6 tons biomass/day). The independence of the accuracy of the model on mesh resolution and computational particle number was determined. The impacts of the particle size distributions (PSD) and drag models on the reactive flows were also investigated.

1. Introduction

Fossil fuels are the primary energy source in industry. These natural resources, however, are limited and will be depleted in the future. Biomass as a renewable energy source can be an alternative to fossil fuels [1–5]. Biomass resources are abundant and can be derived from many sectors such as agricultural residues, food waste, and industrial by-products [6].

Bioenergy can be released from biomass through thermal conversion technologies such as pyrolysis, gasification, and combustion [7,8]. Among these technologies, biomass gasification is an attractive option, because it can generate heat and can also be applied to produce syngas for electricity generation and chemical synthesis. A variety of gasification technologies such as fixed-bed, fluidized-bed, and entrained-flow gasifiers have been developed and applied in various industries [9–11].

Compared to other types of gasification processes, fluidized-bed gasification is attractive due to its efficient mass and energy transfer [12–15]. However, because of the complexity of gas-particle interactions and gasification reaction kinetics, designing fluidized-bed gasifiers is arduous. In recent years, owing to the developments of computer technologies, computational fluid dynamics (CFD) is now capable of simulating biomass gasification to assist with process design, scale-up, and optimization. Currently, there are mainly three CFD methods for the simulations of fluidized-bed biomass gasifiers: the Eulerian–Eulerian (EE) approach, the Eulerian–Lagrangian (EL) approach, and the hybrid Eulerian–Lagrangian approach.

In the Eulerian–Eulerian approach, the particle phase is treated as a continuum. The Eulerian–Eulerian approach requires less computing power because it treats particles as a continuous phase and does not track each of them. Due to its computational effectiveness, this method can be used to simulate large-scale fluidized-bed

* Corresponding author. Tel.: +1 858 5342984.
E-mail address: rjcat@ucsd.edu (R.J. Cattolica).

http://dx.doi.org/10.1016/j.apenergy.2015.09.065
0306-2619/

Nomenclature

A_p	particle surface area (m^2)
$C_{p,i}$	concentration of particle species i ($kmol/m^3$)
C_V	specific heat (kJ/(kg K))
D_t	turbulent mass diffusivity (m^2/s)
D_p	aerodynamic drag function
E	Enthalpy (kJ/kg)
f	particle size distribution function
F	interphase force between the gas and particle phases
g	gravity (m/s^2)
k_d	the thermal conductivity of the particle phase (W/(m K))
δm_p	mass source term ($kg/(m^3\ s)$)
Mw	molecular weight (kg/mole)
Nu	Nusselt number
Re	Reynolds number
u	velocity (m/s)
V	computational cell volume (m^3)
Y_i	mass fraction of gas species i

Greek symbols

α	volume fraction
δ_{ij}	unit tensor
λ_{mol}	the molecular conductivity of the gas phase (W/(m K))
λ_{eddy}	the turbulent conductivity of the gas phase (W/(m K))
ρ	density (kg/m^3)
τ	shear stress tensor ($kg/(m\ s^2)$)
τ_D	particle collision damping time (s)
μ_{lam}	laminar viscosity (m^2/s)
μ_t	turbulent viscosity (m^2/s)

Subscripts

c	char
cp	close packing
g	gas phase
$i,\ j$	coordinate index
p	particle phase

reactors. The EE method, however, has limitations. Because of the assumption of the continuous solid phase, the particle diameters in one solid phase must remain the same and cannot change during the simulation [16]. This can be a serious problem for the simulations of biomass gasifiers in which particle diameters change significantly due to particle surface reactions.

The EL approach can be a better option, because each particle is tracked and has its own properties such as diameter, density, and temperature. The simulations using the EL method, however, are time-consuming. The calculations for particle collisions in dense phase require an enormous amount of computational resources. Therefore, the EL approach may not be suitable for the simulations of industrial fluidized-bed reactors which generally contain millions or billions of particles [17,18].

To simulate dense particle flows more efficiently, a hybrid Eulerian–Lagrangian approach, the Multiphase Particle-In-Cell method (MP-PIC), was developed by Andrews and O'Rourke [19]. In this method real particles are grouped into computational particles and then each computational particle is tracked. In the MP-PIC method one computational particle can represent hundreds or thousands of real particles. The particles defined in one computational particle share the same size, density, velocity, and temperature. Compared to the general EL approach, the MP-PIC method is more computational-efficient.

Furthermore, unlike the EL approach in which particle collisions are calculated by the particle collision models, the effect of particle collision in the MP-PIC method is described by an isotropic solid stress, a function of solid volume fraction [19,20]. This technique avoids intense computation for particle collisions and saves a significant amount of computing time. There are also limitations in the MP-PIC method. This method is not suitable for the simulation of particle bridging, de-fluidized beds, and non-aerated hopper flows in which the direct collisions and inter-particle contacts are critical, because in the MP-PIC method the interactions of particles are calculated with a solid stress model, rather than the collision models. For such cases, the general EL method may be a better option.

Numerous CFD models using the EE, EL, and hybrid EL approaches were previously developed to simulate fluidized-bed gasifiers, but most of them were only focused on one key-component of the fluidized bed system such as a gasifier [20–28]. Other components of the fluidized-bed system such as the cyclone separator and the loop-seal were neglected. The interactions between the key components were simplified as inlets or outlets with the fixed conditions. This simplification can cause serious errors, especially for the systems that consist of multiple reactors and cyclone separators [29]. The best solution to the problem is to simulate the full-loop of fluidized-bed system, instead of a part of the system.

Recognizing the limitations of the single-component approach, researchers have recently focused on simulating the full-loop of fluidized-bed system to improve the model accuracy. Nguyen et al. [30] developed a 2D Eulerian–Eulerian model to study the solid circulation in the full-loop of a dual fluidized-bed system. Wang et al. [31] built a 3D model to simulate the hydrodynamics in a circulating fluidized-bed using the EE approach. Other researchers have conducted similar studies by simulating the full-loop of the fluidized-bed system [32–34].

It should be noted that all of the previous full-loop models are "cold models" in which no chemical reactions were considered. Consequently, these models can only be applied to study the hydrodynamics and cannot be utilized to predict the gas production in the gasifier. Currently, "hot" or "reactive" models that simulate the full-loop of a fluidized-bed biomass gasifier have not been demonstrated.

The purpose of this work is to build a model that can simulate both the hydrodynamics and chemical reactions for a dual fluidized-bed system. To provide more comprehensive insight to the design of fluidized-bed gasifiers, a three-dimensional CFD model for a pilot-scale (6 tons/day, 1 MW_{th}) power plant is developed. In this model, the full-loop of a dual fluidized-bed biomass gasification system including a gasifier, a combustor, a cyclone separator, and a loop-seal is simulated using the MP-PIC method. The kinetics of biomass drying and pyrolysis, heterogeneous char combustion and gasification, and homogeneous gas-phase reactions are all included in this model. The momentum, mass, and energy transport equations are coupled with the reaction kinetics to predict the gas production, particle circulation, and reactor temperature within the dual fluidized-bed gasification system.

The predicted gas composition and reactor temperature profiles are compared with experimental data from the pilot power plant for model validation. Case studies of mesh resolution and particle

number are performed to examine the reliability and accuracy of the model. The impact of the particle size distribution (PSD) and drag models on the reactive flows in the dual fluidized-bed system are also investigated.

2. Governing equations

In this CFD model, the gas phase is simulated by the Large Eddy Simulation (LES) while the particle phase is described by the particle acceleration equation. The interphase momentum transfer is modeled by the drag model. The mass and energy transport equations are coupled with the reaction kinetics to simulate biomass gasification in the dual fluidized-bed system.

2.1. Governing equations for the gas phase

The continuity and momentum equations for the gas phase are shown as follows:

$$\frac{\partial(\alpha_g\rho_g)}{\partial t}+\nabla\cdot\left(\alpha_g\rho_g u_g\right)=\delta m_p \tag{1}$$

$$\frac{\partial(\alpha_g\rho_g u_g)}{\partial t}+\nabla\cdot\left(\alpha_g\rho_g u_g u_g\right)=-\nabla p+F+\alpha_g\rho_g g+\nabla\cdot\tau \tag{2}$$

$$\tau=\mu\left(\frac{\partial u_{g,i}}{\partial x_j}+\frac{\partial u_{g,j}}{\partial x_i}\right)-\frac{2}{3}\mu\delta_{ij}\frac{\partial u_k}{\partial x_k} \tag{3}$$

$$\mu=\mu_{lam}+\mu_t \tag{4}$$

$$\mu_t=\frac{1}{2}C\rho_g\Delta^2\sqrt{\left(\frac{\partial u_{g,i}}{\partial x_j}+\frac{\partial u_{g,j}}{\partial x_i}\right)^2} \tag{5}$$

$$\Delta=\sqrt[3]{V} \tag{6}$$

where $C=0.01$ is a model constant.

The species transport equation is applied to solve for the gas composition, shown as follows:

$$\frac{\partial(\alpha_g\rho_g Y_i)}{\partial t}+\nabla\cdot\left(\alpha_g\rho_g u_g Y_i\right)=\nabla\cdot\left(\alpha_g\rho_g D_t\nabla Y_i\right)+\delta m_{react} \tag{7}$$

$$D_t=\frac{\mu}{\rho_g Sc} \tag{8}$$

where $\delta m_{react.}$ is the mass consumption or generation from the chemical reactions, and Sc, the turbulent Schmidt number, is a set as 0.9.

The following energy transport equation is used to calculate the temperature [20]:

$$\frac{\partial(\alpha_g\rho_g E)}{\partial t}+\nabla\cdot\left(\alpha_g\rho_g u_g E\right)=\alpha_g\frac{\partial p}{\partial t}+\alpha_g u_g\cdot\nabla p-\nabla(\alpha_g q)+\Phi+S_{inter}+Q+q_{diff} \tag{9}$$

where Φ is the viscous dissipation, q is the fluid heat flux, S_{inter} is the heat exchange between the gas and particle phases, q_{diff} is the enthalpy diffusion term, and Q is the heat source due to chemical reactions.

$$q=-(\lambda_{mol}+\lambda_{eddy})\nabla T_g \tag{10}$$

$$\lambda_{eddy}=\frac{C_p\mu_t}{Pr_t} \tag{11}$$

where Pr_t is the turbulent Prandtl number as a constant of 0.9.

$$q_{diff}=\sum_{i=1}^{N_s}\nabla\cdot(\alpha_g\rho_g E_i D_t\nabla Y_i) \tag{12}$$

2.2. Governing equations for the particle phase

In the MP-PIC method, the particle acceleration equation is applied to calculate the particle velocity as shown below:

$$\frac{du_p}{dt}=D_p(u_g-u_p)-\frac{\nabla p}{\rho_p}-\frac{\nabla\tau_p}{\rho_p\alpha_p}+g+\frac{\overline{u_p}-u_p}{2\tau_D} \tag{13}$$

where $\overline{u_p}$ is the local mass-averaged particle velocity. The solid stress tensor, τ_p, is modeled as follows:

$$\tau_p=\frac{10P_s\alpha_p^{\beta}}{\max\left[(\alpha_{cp}-\alpha_p),\varepsilon(1-\alpha_p)\right]} \tag{14}$$

where P_s, β, and ε are the model constants.

The solid volume fraction, α_p, is calculated by the following equation:

$$\alpha_p=\iiint f\frac{m_p}{\rho_p}dm_p du_p dT_p \tag{15}$$

The interphase force between the gas and particle phase is calculated as shown below:

$$F=\iiint f\left\{m_p\left[D_p(u_g-u_p)-\frac{\nabla p}{\rho_p}\right]+u_p\frac{dm_p}{dt}\right\}dm_p du_p dT_p \tag{16}$$

To investigate the impact of drag models in the simulation, the Wen–Yu, Wen Yu–Ergun, and Turton–Levenspiel drag models are employed.

The Wen–Yu model is a drag model that is mainly based on a model for a single-particle in an unbounded fluid and is coupled with a fluid volume fraction multiplier accounting for the particle packing effect [35]. In this paper the Wen–Yu model is used for the base case and is defined as follows:

$$D_p=\frac{3}{4}C_d\frac{\rho_g|u_g-u_p|}{\rho_p d_p} \tag{17}$$

$$C_d=\begin{cases}\frac{24}{Re}\alpha_g^{-2.65}, & Re<0.5\\ \frac{24}{Re}\alpha_g^{-2.65}\left(1+0.15Re^{0.687}\right), & 0.5\leqslant Re\leqslant 1000\\ 0.44\alpha_g^{-2.65} & Re>1000\end{cases} \tag{18}$$

In the Wen–Yu model, the aerodynamic drag function, D_p, is calculated by Eq. (17); the drag coefficient for a particle, C_d, is described by the Stokes model [36] at low Reynolds numbers and is set as 0.44 at high Reynolds numbers; it is estimated by the Schiller–Naumann model [37] in the transition region. The fluid volume fraction multiplier is set as $\alpha_g^{-2.65}$.

As indicated by Snider and Banerjee [38], the Wen–Yu model in the MP-PIC method is capable of providing the accurate predictions for dense gas-sold flows. Additionally, the Wen–Yu model has also been used by other researchers for the simulation of the gas-particle systems [20,29,39]. Note that the Wen–Yu model applied in the MP-PIC method is not the same as that used in the Eulerian–Eulerian approach. The Wen–Yu model in the EE method only uses the Schiller–Naumann model and doesn't include other parts of Eq. (18).

The Wen Yu–Ergun drag model proposed by Gidaspow [40] is a drag model blending the Wen–Yu and Ergun functions. Therefore, this drag model consists of three parts: the Wen–Yu model, Ergun model, and the blending function. The Wen Yu–Ergun drag model in the MP-PIC method is defined as:

$$C_d=\begin{cases}D_{Wen\ Yu} & \alpha_p<0.75\alpha_{cp}\\ (D_{Ergun}-D_{Wen\ Yu})\left(\frac{\alpha_p-0.75\alpha_{cp}}{0.85\alpha_{cp}-0.75\alpha_{cp}}\right)+D_{Wen\ Yu}, & 0.75\alpha_{cp}\leqslant\alpha_p\leqslant 0.85\alpha_{cp}\\ D_{Ergun} & \alpha_p>0.85\alpha_{cp}\end{cases} \tag{19}$$

$$D_{Ergun} = \left(\frac{180\alpha_p}{\alpha_g Re} + 2\right)\frac{\rho_g|u_g - u_p|}{\rho_p d_p} \quad (20)$$

The Turton–Levenspiel model is also a model using a single-particle drag function and a fluid volume fraction multiplier. The aerodynamic drag function is calculated by the following equations [41]:

$$D_p = \frac{18u_g f_w}{\rho_p d_p^2} \quad (21)$$

$$f_w = \left[\left(1.0 + 0.173Re^{0.657}\right) + \frac{0.413Re}{24\left(1 + 16.3Re_p^{-1.09}\right)}\right]\alpha_p^{-2.65} \quad (22)$$

The mass conservation for the particle phase is established on the basis of individual computational particle and is calculated by the following equations:

$$\frac{dm_{p,i}}{dt} = \frac{\alpha_g Mw_{p,i}}{\rho_p \alpha_p} m_p \frac{dC_{p,i}}{dt} \quad (23)$$

$$\frac{dm_p}{dt} = \sum_{i=1}^{N}\frac{dm_{p,i}}{dt} \quad (24)$$

$$\delta m_p = -\iiint f\frac{dm_p}{dt}dm_p du_p dT_p \quad (25)$$

$$C_V\frac{dT_p}{dt} = \frac{1}{m_p}\frac{k_d Nu}{d_p}A_p(T_g - T_p) \quad (26)$$

The conservative energy transferred from the particle phase to the gas phase, S_{inter}, is shown as follows [42]:

$$S_{inter} = \iiint f\left\{m_p\left[D_p(u_p - u_f)^2 - C_V\frac{dT_p}{dt}\right] - \frac{dm_p}{dt}\left[E_p + \frac{1}{2}(u_p - u_f)^2\right]\right\}dm_p du_p dT_p \quad (27)$$

2.3. Reaction kinetics

During the gasification process, after biomass is fed to the gasifier, moisture is released from biomass and then char and volatile gases such as CO, CO_2, H_2, CH_4, and C_2H_4 are generated from biomass pyrolysis. Some of char begins to react with gases to generate CO, H_2, and CH_4. The remaining char is transported to the combustor and is burned with O_2. As the bed material particles are circulated within the dual fluidized-bed system, the heat of char combustion is carried back to the gasifier to sustain the endothermic gasification process. In this work, biomass drying and pyrolysis, heterogeneous char reactions, and homogeneous gas-phase reactions are considered.

The biomass feedstock used in the experiment is almond prunings. In this model the biomass sample is defined as $C_{19.82}H_{24.52}O_{11.86}$ for the dry-ash-free biomass. Additionally, for simplicity the minor elements such as N, S, and Cl are not considered in this work.

2.3.1. Biomass drying

Biomass drying process is described as follows:

$$\text{Moisture in Biomass}_{(s)} \rightarrow H_2O_{(g)} \quad (R1)$$

The rate of biomass drying is calculated by the following equation [43]:

$$r_1 = 5.13\times10^{10}\exp\left(\frac{-10585}{T_p}\right)[Biomass] \quad (28)$$

where [*Biomass*] is the molar concentration of biomass per volume.

2.3.2. Biomass pyrolysis

During pyrolysis, biomass, $C_{19.82}H_{24.52}O_{11.86}$, is decomposed into char and volatile gases, as shown below:

$$C_{19.82}H_{24.52}O_{11.86} \rightarrow 5.96CO + 2.95CO_2 + 8.26H_2 + 1.5CH_4 + 0.5C_2H_4 + 8.41\text{Char}\ (\Delta H = 310.01\ \text{kJ}) \quad (R2)$$

The reaction rate of (R2) is calculated by the single-step global reaction mechanism [44], as shown in Eq. (29), and the pre-exponential factor was chosen as 1.49×10^5 to adjust the proper reaction rate for the biomass feedstock used in the experiment. The composition of the volatiles was determined by the proximate and ultimate analysis of the biomass used in the pilot-scale power plant, as proposed by other researchers [45,46].

$$r_2 = 1.49\times10^5\exp\left(\frac{-1340}{T_p}\right)[Biomass] \quad (29)$$

2.3.3. Heterogeneous char reactions

The heterogeneous char reactions are shown as follows:

$$C + O_2 \rightarrow CO_2\ (\Delta H = -393.51\ \text{kJ}) \quad (R3)$$
$$C + H_2O \leftrightarrow CO + H_2\ (\Delta H = 131.29\ \text{kJ}) \quad (R4)$$
$$C + CO_2 \leftrightarrow 2CO\ (\Delta H = 172.46\ \text{kJ}) \quad (R5)$$
$$C + 2H_2 \leftrightarrow CH_4\ (\Delta H = -74.87\ \text{kJ}) \quad (R6)$$

The reaction rates are calculated by the following equations [47,48]:

$$r_3 = 4.34\times10^7\alpha_c T_p\exp\left(\frac{-13590}{T_p}\right)[O_2] \quad (30)$$

$$r_{4f} = 6.36m_c T_p\exp\left(\frac{-22645}{T_p}\right)[H_2O] \quad (31)$$

$$r_{4r} = 5.218\times10^{-4}m_c T_p^2\exp\left(\frac{-6319}{T_p} - 17.29\right)[H_2][CO] \quad (32)$$

$$r_{5f} = 6.36m_c T_p\exp\left(\frac{-22645}{T_p}\right)[CO_2] \quad (33)$$

$$r_{5r} = 5.218\times10^{-4}m_c T_p^2\exp\left(\frac{-2363}{T_p} - 20.92\right)[CO]^2 \quad (34)$$

$$r_{6f} = 6.838\times10^{-3}m_c T_p\exp\left(\frac{-8078}{T_p} - 7.087\right)[H_2] \quad (35)$$

$$r_{6r} = 0.755m_c T_p^{0.5}\exp\left(\frac{-13578}{T_p} - 0.372\right)[CH_4]^{0.5} \quad (36)$$

2.3.4. Homogeneous gas-phase reactions

The following gas-phase reactions are included in this model:

$$CO + 0.5O_2 \rightarrow CO_2\ (\Delta H = -283\ \text{kJ}) \quad (R7)$$
$$H_2 + 0.5O_2 \rightarrow H_2O\ (\Delta H = -241.82\ \text{kJ}) \quad (R8)$$
$$CH_4 + 2O_2 \rightarrow CO_2 + 2H_2O\ (\Delta H = -802.28\ \text{kJ}) \quad (R9)$$
$$C_2H_4 + 3O_2 \rightarrow 2CO_2 + 2H_2O\ (\Delta H = -1323.13\ \text{kJ}) \quad (R10)$$
$$C_3H_8 + 5O_2 \rightarrow 3CO_2 + 4H_2O\ (\Delta H = -2043.20\ \text{kJ}) \quad (R11)$$
$$CO + H_2O \rightarrow CO_2 + H_2\ (\Delta H = -41.17\ \text{kJ}) \quad (R12)$$

The reaction rates are calculated as follows [49–54]:

$$r_7 = 1.3\times10^{11}\exp\left(\frac{-15155}{T_g}\right)[CO][O_2]^{0.5}[H_2O]^{0.5} \quad (37)$$

$$r_8 = 2.2 \times 10^9 \exp\left(\frac{-13110}{T_g}\right)[H_2][O_2] \quad (38)$$

$$r_9 = 5.01 \times 10^{11} \exp\left(\frac{-24417}{T_g}\right)[CH_4]^{0.7}[O_2]^{0.8} \quad (39)$$

$$r_{10} = 1.0 \times 10^{15} \exp\left(\frac{-20808}{T_g}\right)[C_2H_4][O_2] \quad (40)$$

$$r_{11} = 8.6 \times 10^{11} \exp\left(\frac{-15000}{T_g}\right)[C_3H_8]^{0.1}[O_2]^{1.65} \quad (41)$$

$$r_{12} = 2.75\alpha_p \exp\left(\frac{-10079}{T_g}\right)[CO][H_2O] \quad (42)$$

3. Model setup

The data used in this study is from the experiment conducted on a dual fluidized-bed gasification plant with a full-load of 1 MW_{th}, or 6 tons (biomass)/day. The plant was built by West Biofuels, LLC and is located at the Woodland Biomass Research Center, Woodland, California.

Fig. 1a shows the dual fluidized-bed system which consists of a gasifier, a combustor, a cyclone separator, and a loop-seal. As shown in Fig. 1b, biomass is fed at the side of the gasifier while the steam is presented at the bottom. The 1st, 2nd, and 3rd air supplies are injected into the combustor at three locations. Propane and an additional air supply are presented in the middle of the combustor to provide additional heat to control the temperature of the dual fluidized-bed system.

In the experiment, eight temperature sensors were used to monitor the temperatures at the selected heights of 0.66, 1.12, 3.05, and 5.03 m in the gasifier, and 0.55, 1.83, 2.89, and 6.40 m in the combustor. As shown in Fig. 1c, they are labeled as T1, T2, T3, T4, T7, T8, T9, and T10, respectively. The experimental data used in this work is from an early commissioning test performed with a partial load of the pilot plant and is only used for the

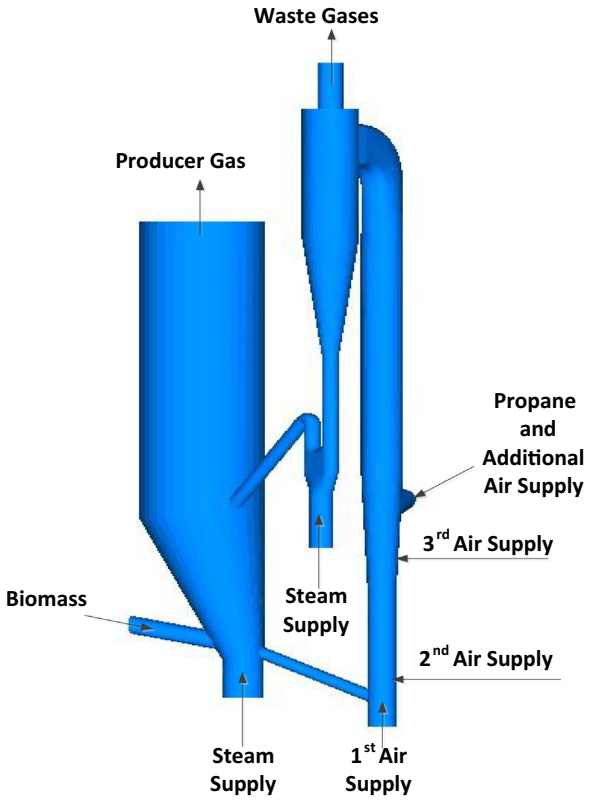

Fig. 1b. Model setup.

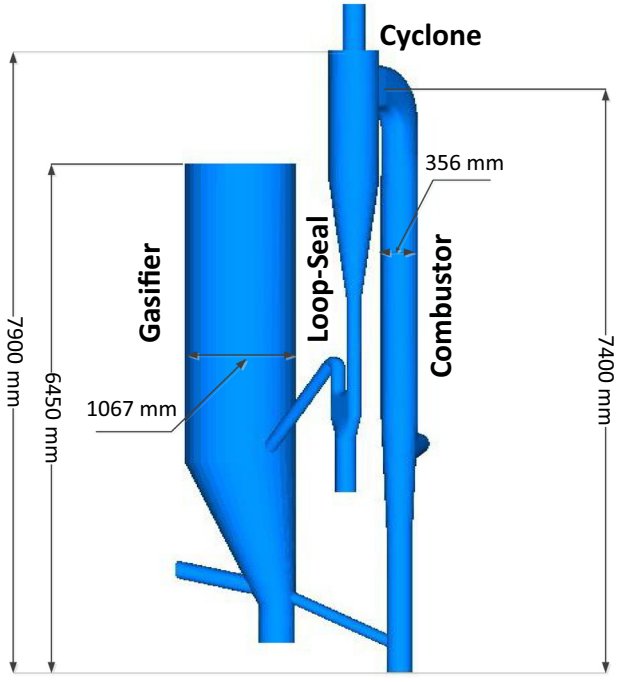

Fig. 1a. Dual fluidized-bed system.

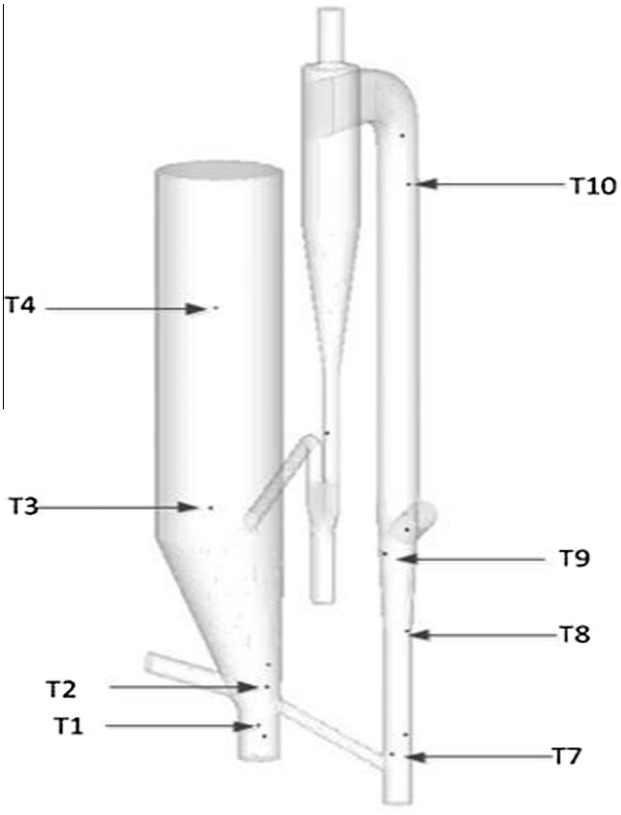

Fig. 1c. Locations of temperature sensors.

purpose of CFD study of biomass gasification. Future studies will include additional operating conditions as they become available.

In this work a comprehensive three-dimensional model is built with the CFD software, Barracuda Virtual Reactor®. A case using a 243,423-cell grid and 419,506 computational particles is set as a base case. The model is set to run for 100 s of simulation time to reach pseudo steady-state. The size of time step is in the range of 10^{-3} to 10^{-5} s and is automatically controlled by the Courant–Friedrichs–Lewy (CFL) scheme to achieve a converged solution. A workstation with an Intel® i7 CPU @3.50 GHz and a GeForce GTX TITAN graphics card is used to perform the computations. Each simulation requires about 96–120 h to be completed. The simulation results are compared with the experimental data to validate the model. The settings of CFD model and the properties of biomass used in the experiment are shown in Tables 1 and 2, respectively.

As shown in Table 1, the mean diameter of bed material particles is 488 μm, and a normal distribution was used for the bed material particles with the standard deviation of 0.146 d_p. The inlet and outlet settings such as mass flow rate, temperature, and pressure are all based on the experimental setup. The thermal wall conditions in Barracuda Virtual Reactor (VR)® are very limited and only two thermal wall conditions such as the prescribed temperature wall and adiabatic wall are available. In the experiment there was heat loss from the gasifier and the amount of the heat loss needed to be calculated due to the large external surface area of the gasifier. In the current model the setting of prescribed wall temperature was applied to the gasifier to simulate heat loss. Meanwhile, as shown in Table 1, the adiabatic wall condition was applied to the combustor, instead of the prescribed temperature wall. The reason is that the effect of the prescribed temperature in Barracuda VR is strong, especially for the small volume of the reactor such as the combustor. The temperature distribution in the combustor can be significantly influenced by the prescribed temperature and even become uniform throughout the combustor, which is unrealistic. Additionally, compared to the gasifier, the amount of heat loss in the combustor is relatively low due to its small external surface area, and therefore the adiabatic wall setting becomes a more reasonable option than the prescribed temperature setting.

Table 1
Model settings.

Bed material properties	
Bed material density (kg/m^3)	3560
Mean diameter of bed material particles (μm), d_p	488
Size distribution of bed material particles	Normal distribution
Standard deviation of the normal distribution	0.146 d_p
Solid volume fraction at close pack	0.56
Initial bed height (m)	2.50
Outlet conditions	
Pressure at the gasifier and cyclone outlets (atm, abs.)	1.0
Mass flow inlet boundary conditions	
Biomass feed rate (kg/h)	72.8
Biomass inlet temperature (K)	293
Mass flow rate of the steam to the gasifier (kg/h)	85.6
Temperature of the steam to the gasifier (K)	640
Mass flow rate of the preheated 1st air to the combustor (kg/h)	36
Temperature of the preheated 1st air to the combustor (K)	602
Mass flow rate of the preheated 2nd air to the combustor (kg/h)	260
Temperature of the preheated 2nd air to the combustor (K)	632
Mass flow rate of the preheated 3rd air to the combustor (kg/h)	362
Temperature of the preheated 3rd air to the combustor (K)	648
Mass flow rate of propane to the combustor (kg/h)	19.5
Temperature of propane to the combustor (K)	293
Pressure of propane to the combustor (Pa)	1.56×10^5
Mass flow rate of the burner air to the combustor (kg/h)	561
Temperature of the burner air to the combustor (K)	293
Mass flow rate of the steam to the loop-seal (kg/h)	27.1
Temperature of the steam to the loop-seal (K)	640
Wall boundary conditions	
Gas phase	No-slip
Particle phase	Partial slip
Thermal boundary condition for the wall of the gasifier	Prescribed wall temperature, 973 K
Thermal boundary condition for the wall of the combustor	Adiabatic wall

Table 2
Biomass properties.

Proximate analysis of biomass sample	
Ash mass fraction, wet basis	0.0209
Fixed C, mass fraction, wet basis	0.2020
Volatile, mass fraction, wet basis	0.7253
Moisture, mass fraction, wet basis	0.0518
Ultimate analysis of biomass sample	
C	0.513
H	0.0529
O	0.409
N	0.0066
S	0.0001
Cl	0.0004
HHV (MJ/kg)	20.1
Biomass density (kg/m^3)	550
Biomass mean diameter (m)	0.0057

As shown in Table 2, the mean diameter of biomass particles is 5.7 mm. In the current work, due to the lack of the data of biomass particle size distribution, the diameter of biomass particles is set as a constant for simplicity. Considering the fact that the major volume of the solids is from the bed material (more than 95%), the assumption of the monodisperse biomass particles may not affect the model accuracy dramatically. However, the size distribution for biomass particles can be included in future studies to improve the model accuracy if the data on the size distribution are available.

4. Results and discussion

4.1. Simulation results

In Fig. 2 the particle circulation in the dual fluidized-bed system is presented in terms of particle volume fraction. In the gasifier the particles are fluidized by the steam and are delivered to the combustor. Then the particles are fluidized by the air and are entrained from the combustor into the cyclone separator. The particles disengage from the gas in the cyclone separator and fall down into the loop-seal. The particles are fluidized by the steam in the loop-seal and are finally transported back to the gasifier.

Fig. 3 shows the view of solid volume fraction in the center of the gasifier and combustor. As seen in the figure, the volatile gases are released from biomass pyrolysis after biomass is fed at the side of the gasifier. Meanwhile, the steam is presented at the bottom of the gasifier and forms bubbles to fluidize the bed material. In the combustor, the air is injected into the combustor to fluidize the bed material and react with the char entrained from the gasifier. The typical "core-annulus" solid structure, dense solid flows in

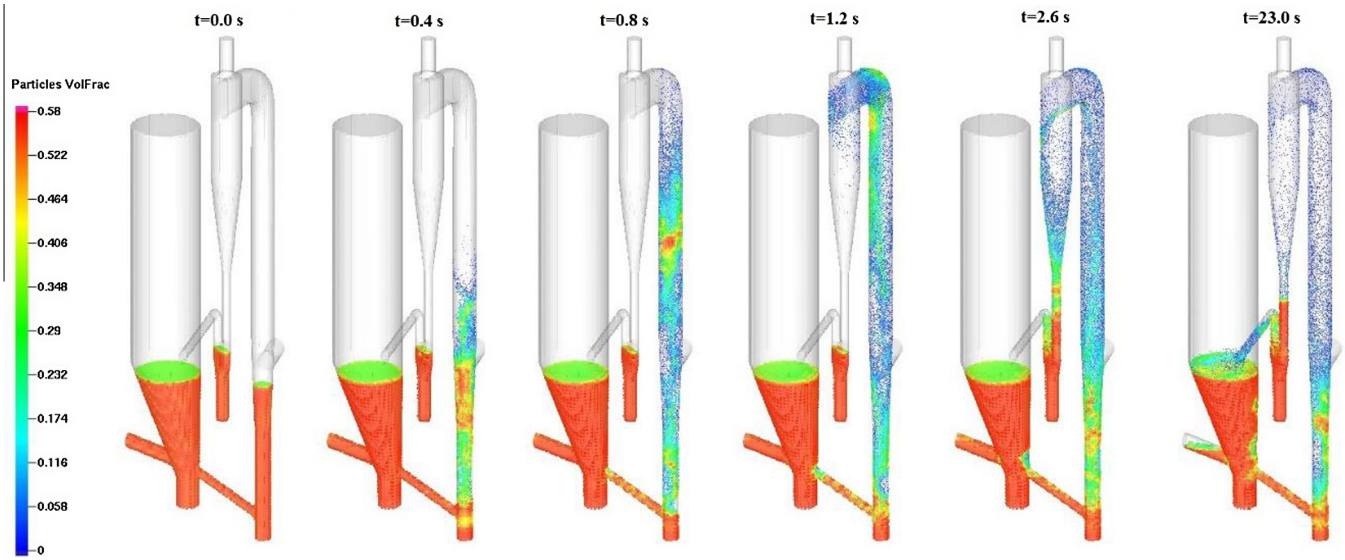

Fig. 2. Particle circulation in the dual fluidized-bed system.

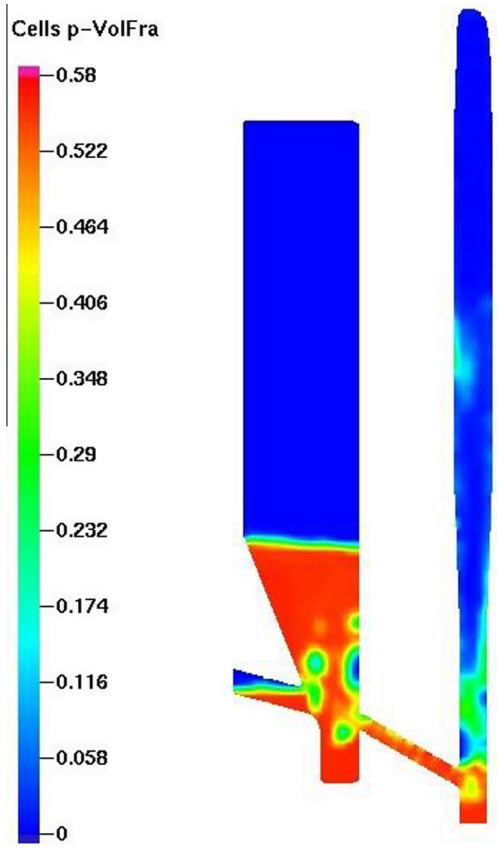

Fig. 3. Section view of solid volume fractions.

the near-wall region and dilute solid flows in the center, is observed in the lower region of the combustor.

In Fig. 4 the gas concentration distributions in the gasifier and combustor are presented. As seen in the figure, H_2 and CO are generated from biomass pyrolysis at the side of the gasifier and then the gases begin to react with char and other gases while penetrating through the bed material. In the meantime, the steam rises up from the bottom of the gasifier to fluidize the bed material. It is also observed that a small amount of steam escapes from the gasifier to the combustor due to the pressure difference; however, no other gases are seen leaking to the combustor. It appears that in the dual fluidized-bed system the steam is not only a fluidization medium and a reactant but also a sealing gas that can prevent other gases escaping from the gasifier to the combustor. Due to the presence of the sealing gas or the steam, the valuable gases such as CO and H_2 can be kept in the gasifier to be further delivered to the downstream unit.

4.2. Study of mesh resolution

Three case studies are conducted to examine how the simulation results are affected by the mesh resolution. The simulation results based on three grids with 216,972, 243,423, and 348,768 cells are compared to each other. As shown in Fig. 5, the predicted gas compositions from the three cases are almost identical. Figs. 6 and 7 show that the predicted reactor temperatures for the three cases are also close and the temperature differences are less than 10 degrees in average.

The comparison results show that the model predictions are not affected dramatically by the mesh resolutions, indicating that the grid resolution for the base case is sufficient for the model to present the accurate results. Accordingly, the 243,423-cell grid is chosen for the remaining studies.

4.3. Study of computational particle number

In the MP-PIC method all of particles are grouped into computational particles and each computational particle is tracked. The calculations of momentum, mass and energy transfer for the particle phase are on the basis of computational particles, rather than real particles.

Applying a large number of computational particles can help to improve the model accuracy, but it also requires a large amount of computing power and the simulation can become very slow; however, if the computational particle number is too small, the accuracy of the model can be compromised. Therefore, it is necessary to implement a study to examine the effect of the computational particle number.

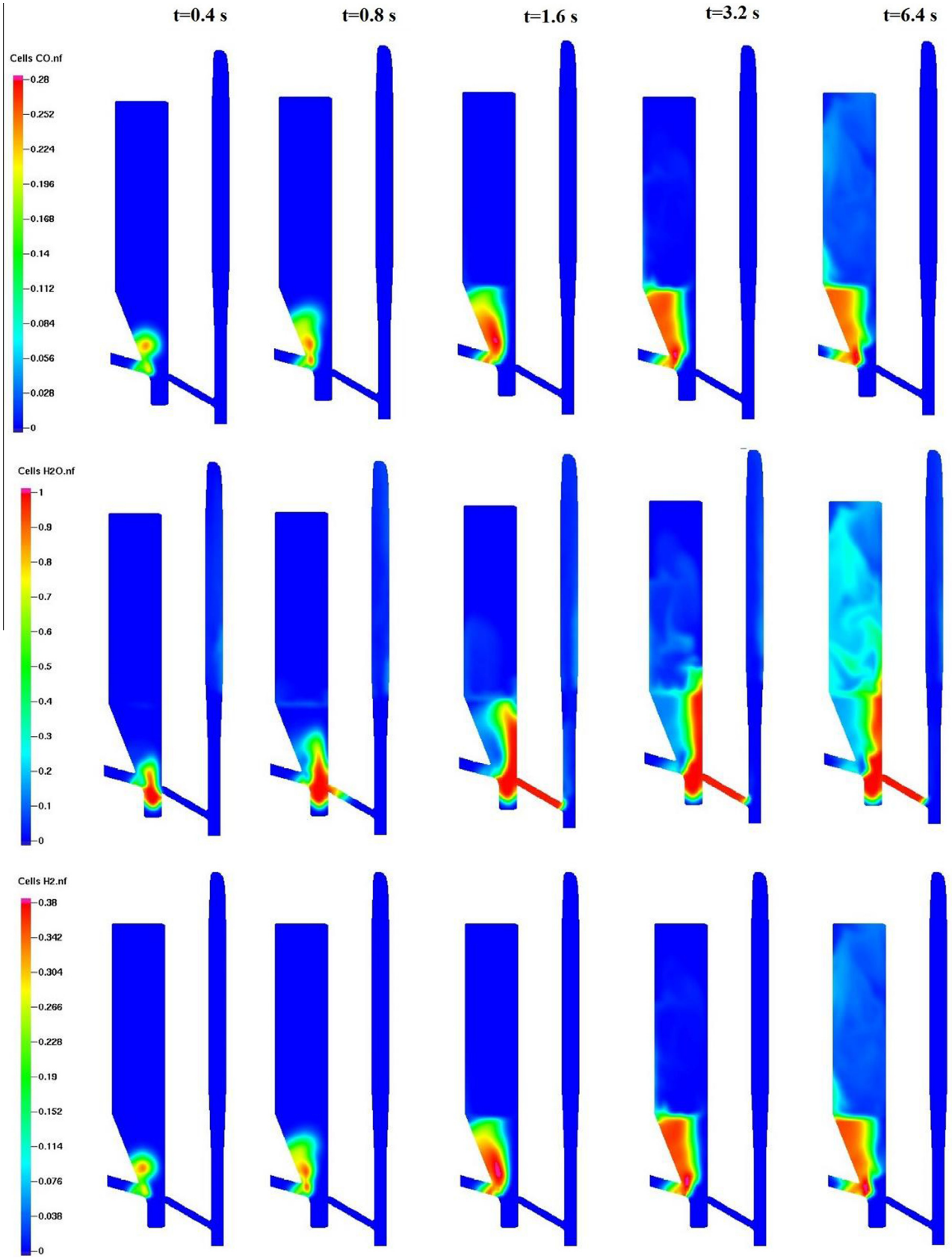

Fig. 4. CO (top), H_2O (middle), and H_2 (bottom) distributions.

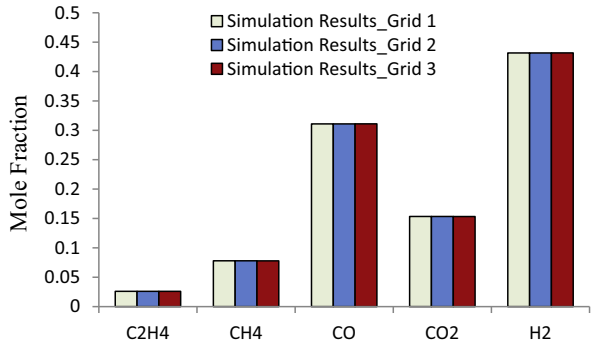

Fig. 5. Gas composition comparison for mesh resolution study.

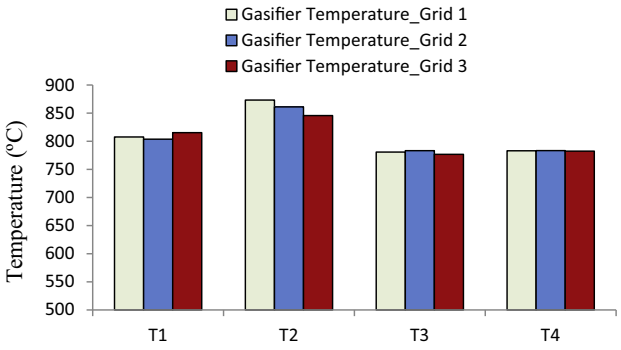

Fig. 6. Gasifier temperature comparison for mesh resolution study.

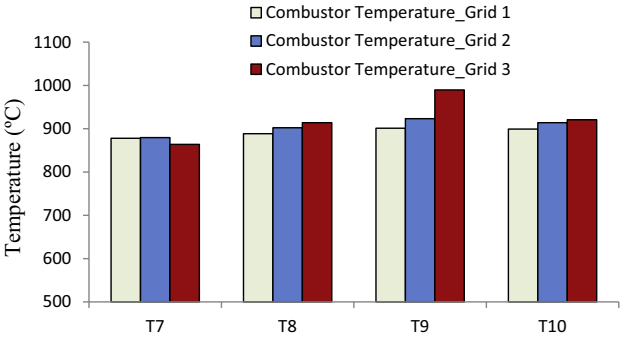

Fig. 7. Combustor temperature comparison for mesh resolution study.

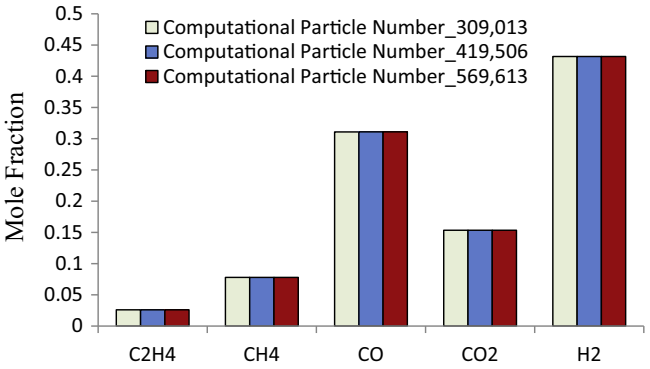

Fig. 8. Gas composition comparison for particle number study.

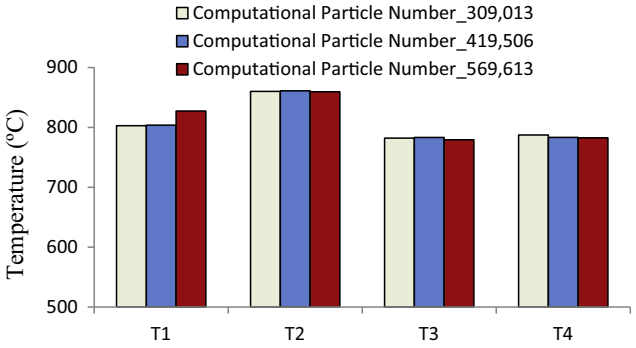

Fig. 9. Gasifier temperature comparison for particle number study.

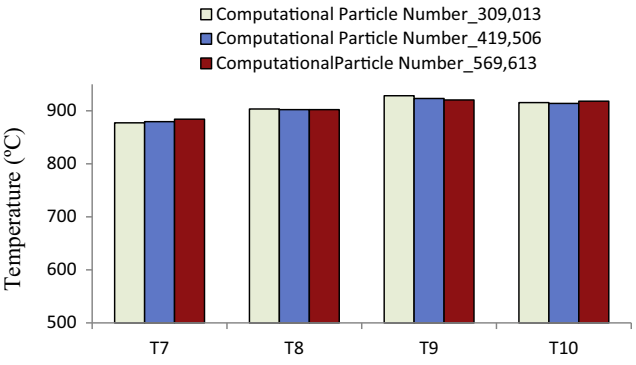

Fig. 10. Combustor temperature comparison for particle number study.

In addition to the base case with 419,506 computational particles, two more cases with 309,013 and 569,613 computational particles are built to investigate the impact of computational particle number on the predictions of gas composition and reactor temperature. As shown in Figs. 8–10, the gas compositions from three cases are almost identical, and the predicted gasifier and combustor temperatures from three cases are similar. The comparison results indicate that the model predictions are not influenced significantly by the computational particle numbers. Therefore, the computational particle number for the base case is sufficient in regard to the model accuracy. Consequently, the computational particle number of 419,506 is selected for the remaining studies.

4.4. Comparison of simulation results and experimental data

In Fig. 11, the predicted concentrations of H_2, CO, CO_2, CH_4, and C_2H_4 are compared with experimental data. As seen in the figure, good agreement is achieved between the predicted gas composition and experimental data. In addition to the comparison of gas composition, the predicted temperatures in the bottom, lower, middle, and upper regions of the gasifier and combustor are compared with the temperature measurements to further examine the model accuracy. As displayed in Figs. 12 and 13, the predicted gasifier and combustor temperatures agree well with the temperature data.

4.5. Study of particle size distribution (PSD)

In fluidized-bed systems, the hydrodynamic regime of the gas-particle system can be greatly influenced by the particle size distribution (PSD). In the current dual fluidized-bed system, there are two types of particles: biomass and bed material particles. As mentioned previously, biomass particles in this model were set as

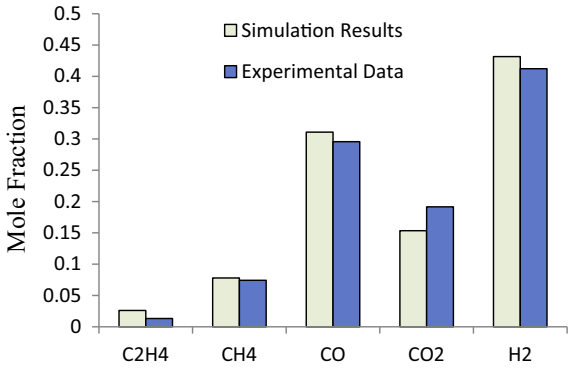

Fig. 11. Producer gas composition comparison (dry basis).

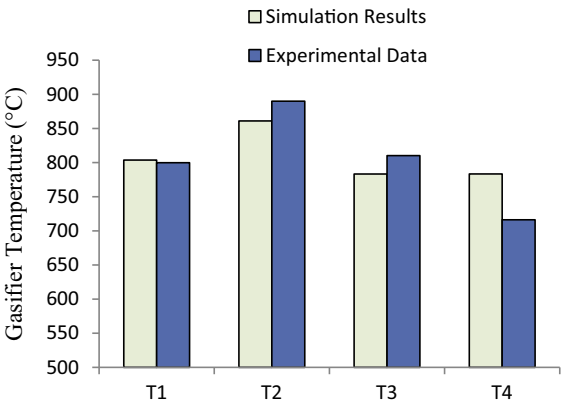

Fig. 12. Gasifier temperature comparison.

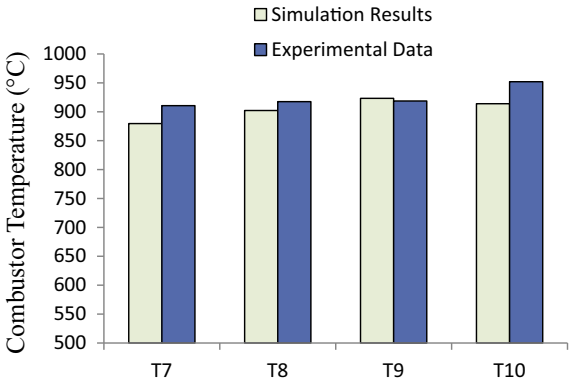

Fig. 13. Combustor temperature comparison.

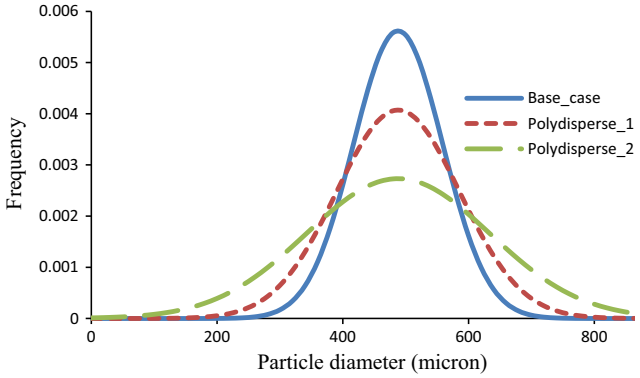

Fig. 14. Particle size distribution (PSD).

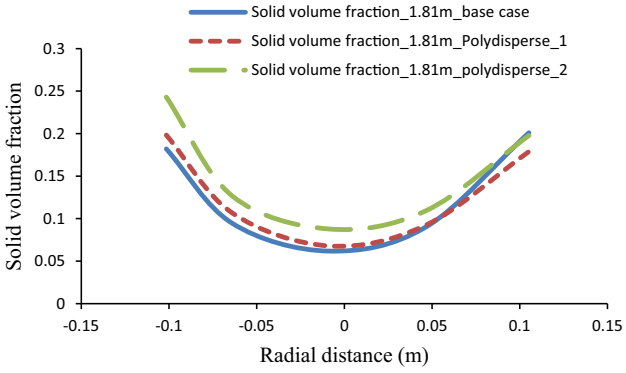

Fig. 15a. Time-averaged solid volume fraction profile at the height of 1.81 m.

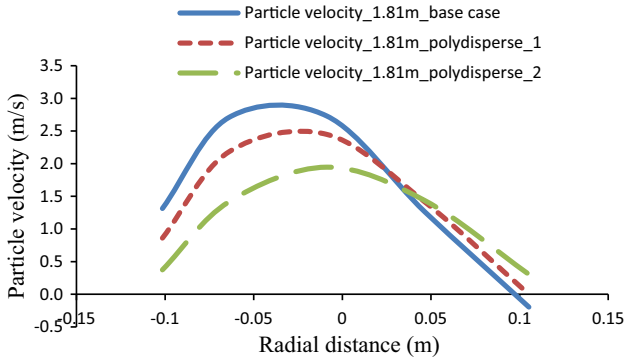

Fig. 15b. Time-averaged particle velocity profile at the height of 1.81 m.

monodisperse particles for simplicity. Considering the fact that most of the solids in the dual fluidized-bed system are bed material particles, only the impact of PSD of the bed material was considered and the PSD for biomass particles was not included in this study.

For the base case, the normal distribution with the standard deviation of 0.146 d_p was applied to the bed material particles as the initial condition. In this section, two more cases using different PSDs are compared with the base case to examine the impact of PSD. The normal distribution function is defined as follows:

$$f_{init} = \frac{1}{\sigma\sqrt{2\pi}} e^{-\frac{(d-d_m)^2}{2\sigma^2}} \quad (43)$$

where d_m is the mean diameter, and σ is the standard deviation. In this section, σ is set as 0.2 and 0.3 of d_m for the cases of polydisperse_1 and polydisperse_2, respectively. As demonstrated in Fig. 14, when σ becomes larger, the range of particle diameter also gets wider.

Fig. 15a displays the time-averaged radial profile of solid volume fraction at the height of 1.81 m for the combustor. As seen in the figure, the solid volume fraction predicted from the case with $\sigma = 0.3d_m$ (polydisperse_2) is higher than those of the case of $\sigma = 0.2d_m$ (polydisperse_1) and the base case. Additionally, as shown in Fig. 15b, the velocity for the case of polydisperse_2 is mostly smaller than those of other two.

The higher solid volume fraction in the case of polydisperse_2 may be caused by the larger value of σ in the PSD. As mentioned

previously, if a larger σ is applied to the PSD, the percentages of small and big particles will become larger. Based on the current hydrodynamic settings, small or mean diameter particles can be moved up quickly; however, big particles may not be lifted up easily and may remain in the lower part of the combustor and accumulate in the near-wall region. Meanwhile, due to the heavy masses of big particles, the particle velocity in the lower region becomes slower than those of other cases. The fact that the flow patterns of three cases are dramatically different indicates that the impact of PSD is significant in the lower region of the combustor.

Figs. 16a and 16b show the profiles of solid volume fraction and particle velocity at the height of 6.62 m in the combustor. As seen in the figures, the dramatic differences of flow patterns observed in the lower region are not seen in the upper region. On the contrary, the profiles of three cases are very close. It may be because the large particles assigned by the PSD tend to stay in the lower region and have difficulty in reaching the higher level to influence the flow pattern. Consequently, the impact of the PSD becomes insignificant in the upper region.

4.6. Study of drag model

In the Eulerian–Eulerian approach, the Wen–Yu model is preferable for dilute gas–solid flows while the Wen Yu–Ergun or Gidaspow model is more universal and used for both dilute and dense gas–solid flows. In the current work the Wen–Yu drag model was chosen for the base case. The reason is that the Wen–Yu model in the MP-PIC method, as mentioned previously, is not the same as that used in the EE approach and can also be used for dense gas–solid flows [20,29,38,39]. However, to further examine the impact of different drag models in the MP-PIC method, the flow patterns from three cases using the different drag models such as the Wen–Yu, WenYu–Ergun, and Turton–Levenspiel models are compared in this section.

Fig. 17a displays the solid volume fractions from three drag models at the height of 1.81 m. All of three models are capable of predicting the core-annulus flow structure at the height of 1.81 m in the combustor. The predicted profiles from three drag models are different from each other. The solid volume fraction predicted by the Wen Yu–Ergun model is higher than other two models. The prediction from the Wen–Yu is smaller than the Wen Yu–Ergun model; however, the difference between the Wen–Yu and Wen Yu–Ergun models is not significant. The Turton–Levenspiel model presents the most dilute solid concentration. Meanwhile, as shown in Fig. 17b, the particle velocities predicted by the three drag models are mostly close to each other.

Fig. 18a shows the solid volume fractions at the height of 3.58 m. As seen in the figure, the predicted solid volume fractions from the Wen–Yu and Wen Yu–Ergun models almost overlap and are both higher than the Turton–Levenspiel model. In Fig. 18b, the particle velocities predicted by the Wen–Yu and Wen Yu–Ergun are also similar and are both lower than the Turton–Levenspiel model.

In Fig. 19a, the predicted solid volume fractions at the height of 6.62 m predicted from three drag models are compared to each other. The solid concentration in the upper region of the combustor becomes dilute and the predictions from all of three models mostly overlap each other. Additionally, as displayed in Fig. 19b, the predicted particle velocities from the Wen–Yu and Wen Yu–Ergun are almost identical and are both slightly lower than that of the Turton–Levenspiel model.

According to the comparison in the lower, middle, upper regions, it is observed that the Turton–Levenspiel model tends to

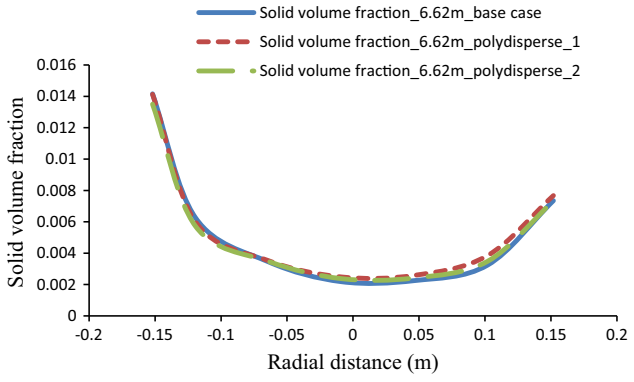

Fig. 16a. Time-averaged solid volume fraction profile at the height of 6.62 m.

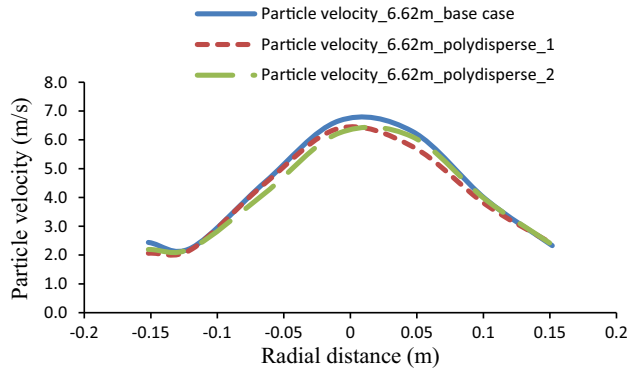

Fig. 16b. Time-averaged particle velocity profile at the height of 6.62 m.

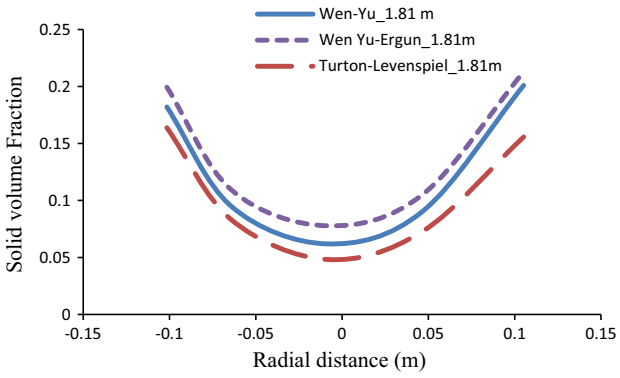

Fig. 17a. Time-averaged solid volume fraction profile at the height of 1.81 m.

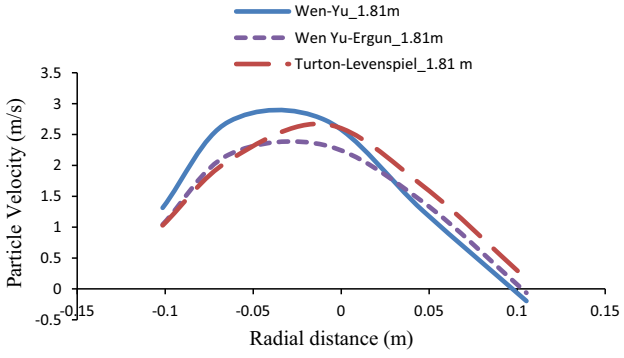

Fig. 17b. Time-averaged particle velocity profile at the height of 1.81 m.

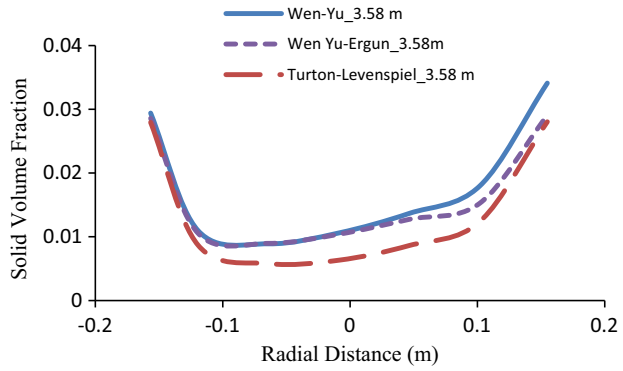

Fig. 18a. Time-averaged solid volume fraction profile at the height of 3.58 m.

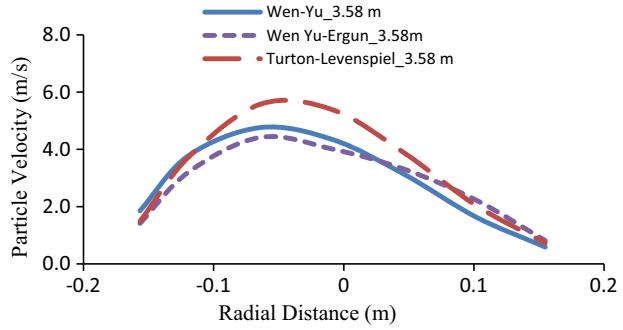

Fig. 18b. Time-averaged particle velocity profile at the height of 6.62 m.

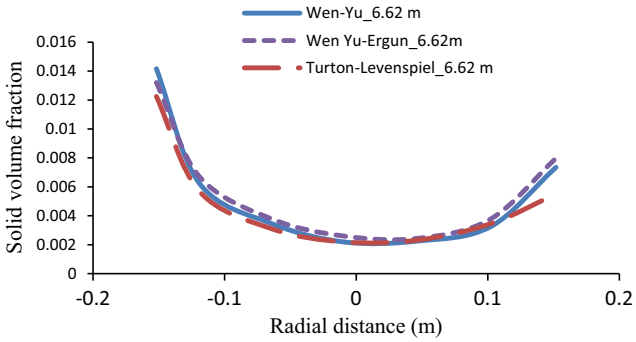

Fig. 19a. Time-averaged solid volume fraction profile at the height of 6.62 m.

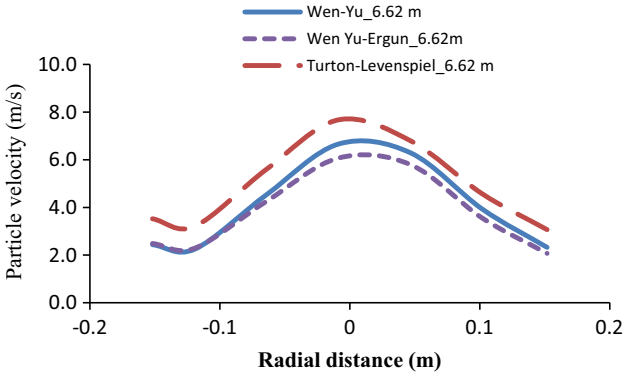

Fig. 19b. Time-averaged particle velocity profile at the height of 6.62 m.

present more dilute solid concentration than the others; both of the Wen–Yu and Wen Yu–Ergun models predict slightly denser solid volume fraction and the difference between the Wen–Yu and Wen Yu–Ergun models is minor. In addition, the results from the current CFD model indicate that the gas compositions are not significantly affected by the different drag models with the gas compositions varying in less than 1%. The reason is that the flow patterns of the three drag models are very close to each other, and consequently, the gas compositions are not affected dramatically. Furthermore, the gas composition is determined primarily by the factors such as the kinetics of heterogeneous and homogeneous reaction, reactant and product concentrations, particle size, reactor residence time, and flow pattern. Therefore, the minor changes in flow patterns with the drag models do not affect the final prediction of gas composition significantly. It is also worth noting that the impact of drag model on the prediction of gas composition and reaction kinetics is a complicated topic and it is very hard to explain in detail how the gas production can be affected by the drag model without sufficient experimental data. Due to the complexity of this issue, the current study is only focused on the hydrodynamic impact of the drag model and the detailed study about the effect of drag model on gas production in the dual fluidized-bed system is not included in this work.

5. Conclusions

In this paper the MP-PIC method was applied to simulate biomass gasification in a dual fluidized-bed system. The predicted gas composition and reactor temperature profiles were compared with the experimental data to validate the model and good agreement was achieved. The studies of mesh resolution and computational particle number were implemented to examine the model accuracy. The base case with the 243,423-cell grid and 419,506 computational particles was chosen for the remaining studies producing acceptable accuracy while minimizing computing cost.

The effect of particle size distribution (PSD) was investigated. In the lower region of the combustor, the solid volume fraction predicted from the case with $\sigma = 0.3d_m$ is higher than those of the case of $\sigma = 0.2d_m$ and the base case, which indicates that the impact of PSD is significant in the lower region; however, the study also shows that in the upper region the impact of PSD becomes insignificant, and the solid volume fractions for the three cases are similar. This is principally because at the current hydrodynamic conditions most of the large particles in the PSD cannot reach the upper region of the combustor to change the flow pattern. Note that due to the lack of experimental data, the impact of biomass PSD is not considered in this work for simplicity; however, it can be included in our future studies if the sufficient experimental data are available.

Three cases using the Wen–Yu, Wen Yu–Ergun, and Turton–Levenspiel drag models were established to examine the impact of the drag models. The profiles of solid volume fraction and particle velocity from three cases were compared. It was found that the solid volume fractions predicted by the Wen–Yu and WenYu–Ergun models were slightly denser and the predicted particle velocities both tended to be smaller than the Turton–Levenspiel model. In the meantime, the difference between the Wen–Yu and Wen Yu–Ergun models is small, indicating that the roles of these two drag models in the MP-PIC method are similar.

It should be noted in the current model all of reactions are simulated by the global reaction scheme. Due to the limitation of the global reaction scheme, the validity of the reaction kinetics in the current model might not be well-kept for other types of biomass feedstock or the systems that are dramatically different from the

current one. In future studies, the detailed kinetics will be evaluated in the context of changing biomass feedstock.

Acknowledgements

The authors gratefully acknowledge the financial support from the California Energy Commission Grant (PIR-11-008) through West Biofuels. Additional support was provided by the University of California Discovery Pilot Research and Training Program (Award 211974).

References

[1] Hubbard WG. Wood bioenergy. In: Dahiya A, editor. Bioenergy. Boston: Academic Press; 2015. p. 55–71 [chapter 4].
[2] Pennington D. Bioenergy crops. In: Dahiya A, editor. Bioenergy. Boston: Academic Press; 2015. p. 111–34 [chapter 7].
[3] Smith LL, Allen DJ, Barney JN. Yield potential and stand establishment for 20 candidate bioenergy feedstocks. Biomass Bioenergy 2015;73(0):145–54.
[4] Williams CL, Dahiya A, Porter P. Introduction to bioenergy. In: Dahiya A, editor. Bioenergy. Boston: Academic Press; 2015. p. 5–36 [chapter 1].
[5] Biberacher M, Tum M, Günther KP, Gadocha S, Zeil P, Jilani R, et al. Availability assessment of bioenergy and power plant location optimization: a case study for Pakistan. Renew Sust Energy Rev 2015;42(0):700–11.
[6] John Hay F. Entrepreneurial opportunities in bioenergy. In: Dahiya A, editor. Bioenergy. Boston: Academic Press; 2015. p. 565–77 [chapter 37].
[7] Manara P, Zabaniotou A. Indicator-based economic, environmental, and social sustainability assessment of a small gasification bioenergy system fuelled with food processing residues from the Mediterranean agro-industrial sector. Sust Energy Technol Assess 2014;8(0):159–71.
[8] Meier D, van de Beld B, Bridgwater AV, Elliott DC, Oasmaa A, Preto F. State-of-the-art of fast pyrolysis in IEA bioenergy member countries. Renew Sust Energy Rev 2013;20(0):619–41.
[9] Hernández JJ, Aranda-Almansa G, Bula A. Gasification of biomass wastes in an entrained flow gasifier: effect of the particle size and the residence time. Fuel Process Technol 2010;91(6):681–92.
[10] Kern S, Pfeifer C, Hofbauer H. Gasification of wood in a dual fluidized bed gasifier: influence of fuel feeding on process performance. Chem Eng Sci 2013;90(0):284–98.
[11] Li J, Liao S, Dan W, Jia K, Zhou X. Experimental study on catalytic steam gasification of municipal solid waste for bioenergy production in a combined fixed bed reactor. Biomass Bioenergy 2012;46(0):174–80.
[12] Diniz Filho PT, Silveira JL, Tuna CE, Lamas WdQ. Energetic, ecologic and fluid-dynamic analysis of a fluidized bed gasifier operating with sugar cane bagasse. Appl Therm Eng 2013;57(1–2):116–24.
[13] Karatas H, Olgun H, Akgun F. Experimental results of gasification of cotton stalk and hazelnut shell in a bubbling fluidized bed gasifier under air and steam atmospheres. Fuel 2013;112(0):494–501.
[14] Murakami T, Asai M, Suzuki Y. Heat balance of fluidized bed gasifier with triple-beds and dual circulation. Adv Powder Technol 2011;22(3):449–52.
[15] Wang X, Lei J, Xu X, Ma Z, Xiao Y. Simulation and experimental verification of a hydrodynamic model for a dual fluidized Bed gasifier. Powder Technol 2014;256(0):324–35.
[16] Gerber S, Behrendt F, Oevermann M. An Eulerian modeling approach of wood gasification in a bubbling fluidized bed reactor using char as bed material. Fuel 2010;89(10):2903–17.
[17] Shi X, Lan X, Liu F, Zhang Y, Gao J. Effect of particle size distribution on hydrodynamics and solids back-mixing in CFB risers using CPFD simulation. Powder Technol 2014;266(0):135–43.
[18] Pepiot P, Dibble CJ, Foust TD. Computational fluid dynamics modeling of biomass gasification and pyrolysis. In: Computational modeling in lignocellulosic biofuel production. American Chemical Society; 2010. p. 273–98.
[19] Andrews MJ, O'Rourke PJ. The multiphase particle-in-cell (MP-PIC) method for dense particulate flows. Int J Multiphase Flow 1996;22(2):379–402.
[20] Snider DM, Clark SM, O'Rourke PJ. Eulerian–Lagrangian method for three-dimensional thermal reacting flow with application to coal gasifiers. Chem Eng Sci 2011;66(6):1285–95.
[21] Yu L, Lu J, Zhang X, Zhang S. Numerical simulation of the bubbling fluidized bed coal gasification by the kinetic theory of granular flow (KTGF). Fuel 2007;86(5–6):722–34.
[22] Wang X, Jin B, Zhong W. Three-dimensional simulation of fluidized bed coal gasification. Chem Eng Process 2009;48(2):695–705.
[23] Cheng Y, Thow Z, Wang C-H. Biomass gasification with CO_2 in a fluidized bed. Powder Technol, in press.
[24] Ku X, Li T, Løvås T. CFD–DEM simulation of biomass gasification with steam in a fluidized bed reactor. Chem Eng Sci 2015;122(0):270–83.
[25] Jeong HJ, Seo DK, Hwang J. CFD modeling for coal size effect on coal gasification in a two-stage commercial entrained-bed gasifier with an improved char gasification model. Appl Energy 2014;123(0):29–36.
[26] O'Rourke PJ, Snider DM. An improved collision damping time for MP-PIC calculations of dense particle flows with applications to polydisperse sedimenting beds and colliding particle jets. Chem Eng Sci 2010;65(22):6014–28.
[27] Liang Y, Zhang Y, Li T, Lu C. A critical validation study on CPFD model in simulating gas–solid bubbling fluidized beds. Powder Technol 2014;263(0):121–34.
[28] Klimanek A, Adamczyk W, Katelbach-Woźniak A, Węcel G, Szlęk A. Towards a hybrid Eulerian–Lagrangian CFD modeling of coal gasification in a circulating fluidized bed reactor. Fuel 2015;152:131–7.
[29] Jiang Y, Qiu G, Wang H. Modelling and experimental investigation of the full-loop gas–solid flow in a circulating fluidized bed with six cyclone separators. Chem Eng Sci 2014;109:85–97.
[30] Nguyen TDB, Seo MW, Lim Y-I, Song B-H, Kim S-D. CFD simulation with experiments in a dual circulating fluidized bed gasifier. Comput Chem Eng 2012;36(0):8–56.
[31] Wang X, Wu X, Lei F, Lei J, Xiao Y. 3D full-loop simulation and experimental verification of gas–solid flow hydrodynamics in a dense circulating fluidized bed. Particuology 2014;16(0):218–26.
[32] Geng C, Zhong W, Shao Y, Chen D, Jin B. Computational study of solid circulation in chemical-looping combustion reactor model. Powder Technol 2015;276(0):144–55.
[33] Guan Y, Chang J, Zhang K, Wang B, Sun Q. Three-dimensional CFD simulation of hydrodynamics in an interconnected fluidized bed for chemical looping combustion. Powder Technol 2014;268(0):316–28.
[34] Peng Z, Doroodchi E, Alghamdi YA, Shah K, Luo C, Moghtaderi B. CFD–DEM simulation of solid circulation rate in the cold flow model of chemical looping systems. Chem Eng Res Des 2015;95(0):262–80.
[35] Wen CY, Yu YH. Mechanics of fluidization. Chem Eng Progr Symp 1966(62):100–10.
[36] White FM. Viscous fluid flow. McGraw-Hill mechanical engineering. McGraw-Hill Education; 2005.
[37] Schiller L, Naumann Z. A drag coefficient correlation. Z Ver Deutsch Ing 1935;77:318.
[38] Snider D, Banerjee S. Heterogeneous gas chemistry in the CPFD Eulerian–Lagrangian numerical scheme (ozone decomposition). Powder Technol 2010;199(1):100–6.
[39] Vivacqua V, Vashisth S, Hébrard G, Grace JR, Epstein N. Characterization of fluidized bed layer inversion in a 191-mm-diameter column using both experimental and CPFD approaches. Chem Eng Sci 2012;80:419–28.
[40] Gidaspow D. Multiphase flow and fluidization. Continuum and kinetic theory description. Boston: Academic Press; 1994.
[41] Turton R, Levenspiel O. A short note on the drag correlation for spheres. Powder Technol 1986;47(1):83–6.
[42] O'Rourke PJ. Collective drop effects on vaporizing liquid sprays. Princeton University; 1981.
[43] Xu J, Qiao L. Mathematical modeling of coal gasification processes in a well-stirred reactor: effects of devolatilization and moisture content. Energy Fuels 2012;26(9):5759–68.
[44] Yu J, Yao C, Zeng X, Geng S, Dong L, Wang Y, et al. Biomass pyrolysis in a micro-fluidized bed reactor: characterization and kinetics. Chem Eng J 2011;168(2):839–47.
[45] Deng Z, Xiao R, Jin B, Huang H, Shen L, Song Q, et al. Computational fluid dynamics modeling of coal gasification in a pressurized spout-fluid bed. Energy Fuels 2008;22(3):1560–9.
[46] Li Q, Zhang M, Zhong W, Wang X, Xiao R, Jin B. Simulation of coal gasification in a pressurized spout-fluid bed gasifier. Can J Chem Eng 2009;87(2):169–76.
[47] Yoon H, Wei J, Denn MM. A model for moving-bed coal gasification reactors. AIChE J 1978;24(5):885–903.
[48] Syamlal M, Bissett LA. METC gasifier advanced simulation (MGAS) model. In Other information: PBD: Medium: ED; Size; January 1992. 91 p.
[49] Howard JB, Williams, GC. Kinetics of carbon monoxide oxidation in postflame gases. In: Proc 14th symp (int) combust; 1973. p. 975–86.
[50] Mitani T, Williams FA. Studies of cellular flames in hydrogen–oxygen–nitrogen mixtures. Combust Flame 1980(39):169–90.
[51] Dryer FL, Glassman I. High-temperature oxidation of CO and CH_4. In: Proc 14th symp (int) combust; 1973. p. 987–1003.
[52] Kaushal P, Pröll T, Hofbauer H. Model development and validation: co-combustion of residual char, gases and volatile fuels in the fast fluidized combustion chamber of a dual fluidized bed biomass gasifier. Fuel 2007;86(17–18):2687–95.
[53] Westbrook CK, Dryer FL. Simplified reaction mechanisms for the oxidation of hydrocarbon fuels in flames. Combust Sci Technol 1981;27(1–2):31–43.
[54] Lu X, Wang T. Water–gas shift modeling in coal gasification in an entrained-flow gasifier. Part 1: development of methodology and model calibration. Fuel 2013;108(0):629–38.